Materials Science-Poland, 40(4), 2022, pp. 14-27
http://www.materialsscience.pwr.wroc.pl/
DOI: 10.2478/msp-2022-0039

Structure and properties of laser-cladded Inconel 625-based in situ composite coatings on S355JR substrate modified with Ti and C powders

Tomasz Poloczek[1,*], Aleksandra Lont[1], Jacek Górka[1]

[1]Silesian University of Technology, Gliwice, Poland

This article presents the research results on the production of laser-cladded Inconel-625 in situ composite coatings on the S355JR substrate by addition of titanium and graphite powders to pure Inconel 625 alloy powder mixture for increased hardness and erosive wear resistance of the coatings. The research featured in the article includes penetrant testing, macro-, and microscopic observations of produced coatings, phase and chemical composition analysis, hardness and solid particle erosion tests. The results showed that the addition of titanium and graphite powders resulted in the composite microstructure formation by precipitation of Ti, Nb, Mo, and C-rich blocky and eutectic particles during crystallization. The conducted tests revealed that the microstructure change resulted in an increase in hardness and erosive wear resistance by 27% and 30%, respectively.

Keywords: *Inconel 625, composite coating, erosive wear, microstructure, hardness*

1. Introduction

Nickel-based alloys and superalloys are widely used in the aerospace, energy, chemical, and petrochemical industries as they show attractive properties that include high-temperature corrosion and oxidation resistance in aggressive environments, high tensile strength and fatigue resistance, together with high toughness and ductility [1]. These materials are not only used as coatings for corrosion resistance improvement of the surface, but currently the research is focused on the possibility of nickel-based composite coatings production in order to achieve both high corrosion and wear resistance of the surface [2]. So far, research has been carried out on the production of nickel-based composite coatings reinforced by carbon materials (graphene nanoplatelets [3], carbon nanotubes [4], and carbon fibers [5]) and carbides (WC [6], TiC [7], NbC [8], TaC [9], Cr_3C_2 [10], B_4C [11]). Mostly, the research has been focused on the ex situ nickel-based composite coatings reinforced by TiC particles due to high properties of those carbides at high temperatures, including high hardness, modulus, high melting temperature, thermal stability, and corrosion resistance. Previous investigations have revealed that the Ni-based composite coatings reinforced by TiC particles present higher hardness, sliding abrasive wear resistance, and friction coefficient as well as resistance to solid particle erosion in comparison to metallic Ni-based coatings [12–16].

As proven in many works, TiC particles can be in situ synthesized by laser surface treatment processes due to low Gibbs energy and high formation temperature. The in situ synthesis in comparison to the ex situ method generally allows to improve the bonding between reinforcement and matrix material which provides higher mechanical properties of the composite coating [17, 18]. It has been proven that by proper selecting and optimizing the laser surface treatment process parameters, it is possible to control the microstructure (TiC particles fraction, size, morphology, and distribution uniformity) and properties of the produced composite coatings or surface layers [19, 20]. However, there are still few research results on the possibility of producing TiC in situ reinforced Ni-based superalloys composite coatings by laser cladding. Shut-

* E-mail: tomasz.poloczek@polsl.pl

© Poloczek et al. 2022. This is an open access article distributed under the Creative Commons Attribution-NonCommercial-NoDerivatives 4.0 License. (http://creativecommons.org/licenses/by-nc-nd/4.0/)

ing et al. [21] tested the laser-cladded Ni45 alloy coatings with addition of pure Nb, Ti, and Cr_3C_2 powders, which resulted in (Ti, Nb)C precipitation in the microstructure. The authors investigated the influence of cooling in liquid nitrogen in comparison to air cooling on the microstructure and properties of coatings. Chen et al. [22] reported the effect of Ti and Ni-coated C particles addition to Ni-based self-fluxing alloy powder for coatings production on the phase composition and microstructure, cracking, porosity, microhardness, and wear resistance. As a result of powder chemical composition change, the authors noted the presence of new phases (TiC, TiB_2, Cr_3C_2, $TiNi_3$, TiNi, Fe_2Ti). Generally, the TiC particles volume fraction depending on the used powder mixture was 10.82–28.06 vol.%, and with the TiC increase, the microhardness and wear resistance improved. Similarly, Gao et al. [23] tested the phase composition, microstructure, microhardness, and tribological properties of the laser-cladded coatings produced using Ni60 alloy with TC4 (Ti, C, Fe, Al) powder mixture. During the laser cladding process, the addition of TC4 powder caused in situ synthesis of the TiB_2, TiC, TiB, Ni_3Ti, and $NiTi_2$ phases. As a result, the authors noted increased microhardness and wear resistance of the coating with 4 wt.% of TC4 powder. Wu et al. [24] tested the effect of Mo addition to powder mixtures composed of Ni60 alloy, C, and TiN for laser cladding composite coatings on their microstructure and properties. As a result of the laser cladding process, they received in situ Ti(C,N) reinforced Ni-based composite coatings. The Mo addition caused microstructure refinement and hardness and wear resistance increased. Muvvala et al. [25] monitored the thermal cycles during laser cladding of Inconel 718-based composite coatings reinforced by in situ synthesized TiC. The increased molten pool lifetime caused the TiC particles to increase and morphology to change from cubic to dendritic and eutectic. The test results showed that finer TiC particles had a beneficial effect on obtaining higher hardness and wear resistance of the coatings.

From the above studies it is clear that using laser cladding technology the Ni-based composite coatings reinforced by TiC may be produced using in situ synthesis and they show improved hardness and wear resistance. For the current study, the Inconel 625-based composite coatings reinforced by in situ synthesized TiC were made and the effect of process parameters and powder composition on the microstructure and properties was tested. The tests included penetrant testing, macrostructure and microstructure observations, X-ray diffraction (XRD) analysis, energy dispersive spectrometer (EDS) analysis, hardness, and solid particle erosion.

2. Experimental

2.1. Materials

For the study, the substrate material surface (100 mm × 50 mm × 10 mm as-received S355JR low-alloy steel) was prepared by grinding, cleaning, and degreasing with ethyl alcohol. The coating precursor material was a powder mixture of gas atomized spheroidal Inconel 625 Ni-based superalloy powder (Oerlikon Metcoclad 625, particle size 45–90 μm), 99.0% pure titanium powder (H.C. Starck AMPERIT 154, particle size 45–70 μm), and 99.5% pure graphite powder (Merck KGaA 1.04206.9025, particle size <50 μm) at volume ratios of 95:2.5:2.5 (P1) and 90:5:5 (P2). The chemical compositions of substrate material and Metcoclad 625 powder are presented in Table 1. The powder mixtures were mixed in a tumbler for 0.5 hr and dried for 1 hr at 50°C prior to the laser cladding process.

2.2. Laser processing

For the laser cladding process, the stand was equipped with a TRUMPF Trudisk 3302 disk laser (Table 2), and a numerically controlled system for positioning the substrate material in relation to laser head and gravitational powder feeding system was used. For the process, the laser beam focus was set 30 mm above the substrate surface and the head was set at an angle of 10° relative to the vertical axis to minimize the risk of beam reflection to the laser head. For the process, argon was used as shielding gas (10 l/min) and powder transporting gas (3 l/min). The powder was injected directly into the molten pool. For the study,

Table 1. Chemical compositions of S355JR substrate material and Metcoclad 625 powder

Material	C	Mn	Si	P	S	Cr
	wt.%					
S355JR	0.2	1.5	0.2–0.5	Max 0.04	Max 0.04	Max 0.3
Oerlikon Metcoclad 625	–	–	–	–	–	20.0–23.0

Material	Ni	Mo	Nb	Al	Cu	Fe
	wt.%					
S355JR	Max 0.3	–	–	Max 0.02	Max 0.03	Balance
Oerlikon Metcoclad 625	58.0–63.0	8.0–10.0	3.0–5.0	–	–	Max 5.0

Table 2. Technical specifications of TRUMPF Trudisk 3302 laser

Property	Value
Wavelength, μm	1.3
Maximum output power, W	3300
Laser beam divergence, mm/rad	<8.0
Fiber core diameter, μm	200
Collimator focal length, mm	200
Focusing lens focal length, mm	200
Beam spot diameter, μm	200
Fiber length, m	20

Table 3. Laser-cladding parameters

Designation	Powder mixture	Laser power, W	Speed, mm/min
P1-1	P1	2,000	240
P1-2	P1	2,150	258
P1-3	P1	2,300	276
P2-1	P2	2,000	240
P2-2	P2	2,150	258
P2-3	P2	2,300	276
P3-1	Metcoclad 625	2,000	240
P3-2	Metcoclad 625	2,150	258
P3-3	Metcoclad 625	2,300	276

a set of multi-pass coatings was prepared using P1 and P2 powder mixtures as well as pure Metcoclad 625 powder with a 40% overlap, where the stitch axis distance was 2.6 mm. The process parameters (Table 3) were chosen based on previous experience [14]. The laser power was set in a range of 2,000–2,300 W, and a speed of 240–276 mm/min, constant heat input of 500 J/mm, and constant powder feed rate of 10 g/min were applied. The laser cladding process was provided without preheating and the interpass temperature was $<30^{\circ}$C.

2.3. Penetrant testing

For verification of the crack presence on the coating surfaces, penetrant testing was carried out using color contrast technique (penetrant MR 68 NF, developer MR 70, cleaner MR 79). Both dwell and development times for penetrant testing were 10 min.

2.4. Macrostructure and microstructure analysis

The coating macrostructure and microstructure were examined by optical microscope Olympus

SZX9 and scanning electron microscopes (SEM) Phenom World PRO equipped with an EDS and SEM ZEISS SUPRA 25. Scanning electron microscopy was conducted in the backscattered electron (BSE) mode. For EDS analysis, a 10-kV accelerating voltage was applied. The specimens were etched using etchant 89 according to ASTM E 407-99 standard [26]: a mixture of HNO_3, HCl, acetic acid, and glycerol. The XRD analysis was conducted with Malvern PANanalytical X'Pert PRO diffraction system with filtered radiation from the lamp using cobalt anode. The diffraction profiles were recorded from the coating ground surfaces in the 2θ range between 30° and 130° in a continuous scan mode with a step size of 0.0263°. The counting time per step was 31.365 s. The coating thickness and dilution level were estimated with the Autodesk AutoCad 2023 software. The dilution was calculated using Eq. (1), were F_{BM} is the melted cross-sectional area of the substrate and RA is the cross-sectional area of reinforcement of the clad. The reinforcing particles volume fraction was estimated using the Image-Pro Plus 4.5.0.29 software on the basis of SEM micrographs:

$$U = \frac{F_{BM}}{F_{BM} + RA} \times 100\ [\%] \tag{1}$$

2.5. Hardness testing

Vickers hardness tests were performed on polished and etched coating cross-sections using FM700 Vickers hardness tester. The tests were performed in three measuring lines across the multi-pass coatings (Figure 1A) and from the surface toward the substrate material (Figure 1B), with a 0.5 mm and 0.2 mm distance between consecutive measuring points, respectively. The hardness was measured using a 500 g load and dwell time of 10 s.

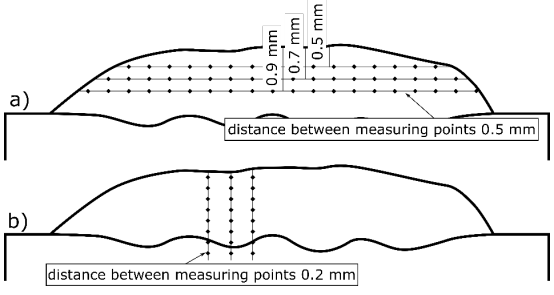


Fig. 1. Vickers hardness lines scheme. (A) Measurements across the multi-pass coating. (B) Measurements from the coating surface toward the substrate material

2.6. Solid particle erosion tests

The solid particle erosion tests were carried out according to the ASTM G76-04 standard [27] on the grounded and cleaned coating surfaces. Testing was performed using 50-μm diameter Al_2O_3 particles in dry air as erodent material for 10 min. The velocity of the abrasive particles was 70 m/s and the feed rate was 2 g/min. The coating surfaces were located 10 mm below the nozzle. The impingement angles of 30° and 90° were applied to provide the maximum conditions for both brittle and ductile materials for each angle, and sample three tests were performed. As a result of erosion tests, the mass loss was measured with a laboratory scale with an accuracy of 0.0001 g and the erosion rates Eq. (2) and erosion values Eq. (3) were calculated. The coating density was measured using the Archimedes method. To assess the erosion mechanism of the tested coatings, crater observations were carried out using SEM ZEISS SUPRA 25:

$$\text{erosion rate} = \frac{\text{mass loss}}{\text{test time}} \quad \left[\frac{\text{mg}}{\text{min}}\right] \tag{2}$$

$$\text{erosion value} = \frac{\text{volume loss}}{\text{total mass of abrasive particles}} \quad \left[\frac{\text{mm}^3}{\text{g}}\right] \tag{3}$$

3. Results and discussion

3.1. Penetrant testing

The coating surface views after penetrant testing are presented in Figure 2. In the case of all tested coatings, no indications were found. The visible coloration around coatings and at craters result from the surface roughness and qualify as a spurious indication. The penetrant tests revealed that the conducted laser cladding process of metallic and composite Inconel 625-based coatings allowed to produce high-quality coatings without surface cracks.

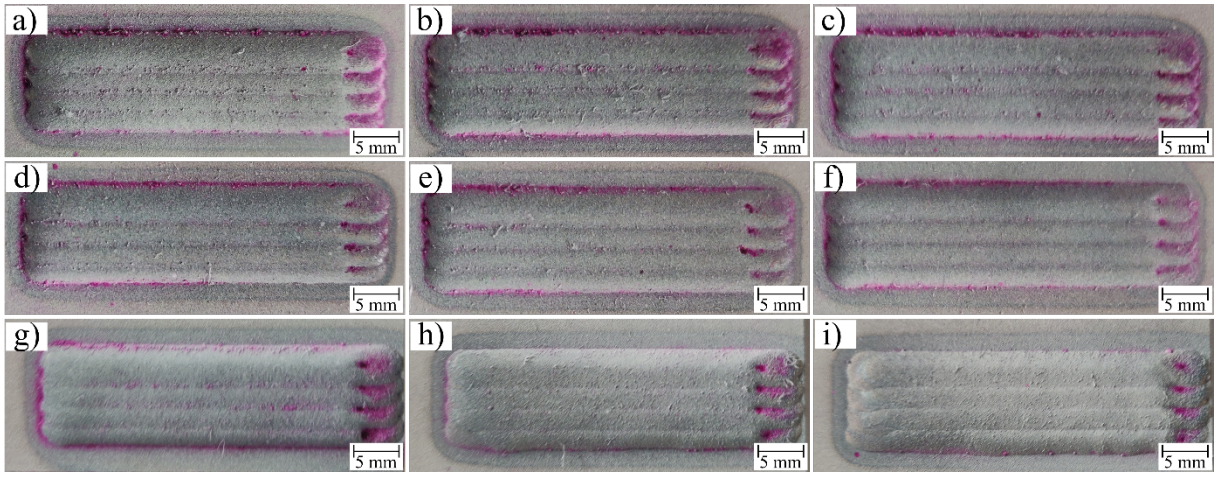


Fig. 2. Penetrant test results of laser-cladded coatings: (A) P1-1; (B) P1-2; (C) P1-3; (D) P2-1; (E) P2-2; (F) P2-3; (G) P3-1; (H) P3-2; and (I) P3-3. *Note*: Designations are according to Table 3

3.2. Macrostructure and microstructure characterization

The macrographs of laser-cladded coatings are shown in Figure 3. All of the coatings are characterized by good metallurgical joining to the substrate and no welding imperfections were observed. The thickness and dilution of coatings together with the measured reinforcing phase volume fraction are presented in Table 4. The average chemical compositions of the coating cross-sectional regions received from EDS are presented in Table 5. Together with the increase in laser beam power and speed (with constant heat input), the coating thicknesses slightly decreased, the penetration and dilution increased, while the reinforcing particles volume fraction decreased. The higher penetration and dilution may be attributed to the higher temperature gradient between the surface and base material due to higher laser beam power, leading to increased intensity of the Marangoni convection. The iron and titanium content results from EDS analysis are in good agreement with the dilution and reinforcing particles volume fraction measurements. As a result of higher penetration, the coating volume increased leading to the increased iron content and decreased reinforcing particles volume fraction and titanium content. With the increased titanium and graphite contents in the powder mixture, the coating thicknesses also slightly decreased. In the case of the composite coatings, the increased titanium and graphite contents caused the penetration and dilution to increase, which can be attributed to the higher radiation absorption level due to the amount of graphite in the mixture. As a result of laser cladding with powder mixture containing 2.5 vol.% and 5.0 vol.% of Ti and graphite, the volume fraction of the reinforcing particles in the composite coatings was 2.6–3.0 vol.% and 4.5–6.4 vol.%, respectively. The average titanium content for coatings produced with the powder mixtures was 2.4–2.8 wt.% and 3.3–4.1 wt.%, respectively. Macroscopic examinations showed no correlation between the processing parameters and coating widths.

The representative SEM images of the microstructure of metallic Inconel 625 coatings that were tested to assess the impact of the titanium and graphite addition to the powder mixture on the microstructure are presented in Figure 4. The SEM micrographs of the composite coatings produced with the addition of titanium and graphite to Inconel 625 powder are presented in Figures 5 and 6. Figure 7 shows the XRD patterns of the metallic Inconel 625 coating and representative composite coating. As can be seen in Figure 4, the metallic Inconel 625 laser-cladded coatings have a typical dendritic microstructure with minor constituents in the interdentritic regions [28, 29]. XRD analysis

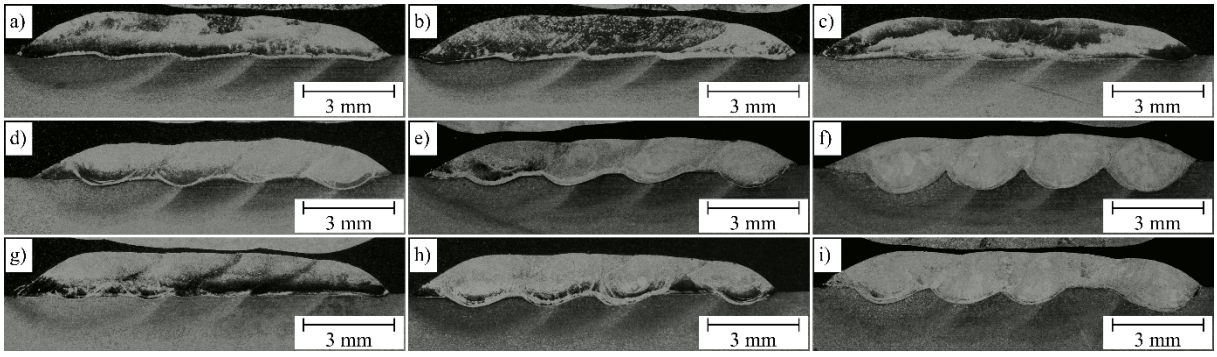


Fig. 3. Macrographs of laser-cladded coatings: (A) P1-1; (B) P1-2; (C) P1-3; (D) P2-1; (E) P2-2; (F) P2-3; (G) P3-1; (H) P3-2; and (I) P3-3. *Note*: Designations are according to Table 3

Table 4. The laser-cladded coating thickness, dilution, and reinforcing particles volume fraction

Designation	**Coatings thickness, mm**	**Dilution, %**	**Reinforcing particles volume fraction, vol.%**
P1-1	1.43 ± 0.2	7.4 ± 0.2	3.0 ± 0.3
P1-2	1.35 ± 0.2	8.5 ± 0.3	2.6 ± 0.5
P1-3	1.22 ± 0.3	8.8 ± 0.4	2.7 ± 0.1
P2-1	1.23 ± 0.2	13.3 ± 0.3	6.4 ± 0.9
P2-2	1.04 ± 0.1	20.0 ± 0.5	5.5 ± 0.2
P2-3	0.95 ± 0.1	30.8 ± 0.3	4.5 ± 0.6
P3-1	1.42 ± 0.3	5.6 ± 0.1	–
P3-2	1.37 ± 0.2	13.3 ± 0.5	–
P3-3	1.16 ± 0.1	22.3 ± 0.3	–

Note: Designations are according to Table 3

Table 5. The average EDS chemical composition of laser-cladded coatings

Designation	**Ni**	**Cr**	**Mo**	**Nb**	**Fe**	**Ti**
	wt.%					
P1-1	56.5 ± 1.8	18.7 ± 0.4	10.7 ± 0.7	4.9 ± 0.6	6.9 ± 1.7	2.4 ± 0.1
P1-2	55.4 ± 2.7	18.3 ± 0.7	10.3 ± 1.0	4.3 ± 0.8	8.9 ± 3.5	2.8 ± 0.2
P1-3	54.4 ± 1.2	18.0 ± 0.4	11.0 ± 0.3	4.7 ± 0.5	9.1 ± 1.3	2.8 ± 0.1
P2-1	48.6 ± 2.5	15.6 ± 0.6	10.2 ± 1.1	5.0 ± 0.8	16.3 ± 5.1	4.1 ± 0.3
P2-2	43.2 ± 5.1	14.5 ± 1.9	9.1 ± 1.0	4.3 ± 0.6	24.8 ± 8.4	4.0 ± 0.5
P2-3	33.3 ± 2.3	11.2 ± 0.6	7.8 ± 0.4	4.0 ± 0.5	40.1 ± 2.7	3.3 ± 0.3
P3-1	60.2 ± 1.6	19.5 ± 0.8	10.5 ± 0.8	4.0 ± 1.5	5.7 ± 0.5	–
P3-2	54.0 ± 1.1	17.7 ± 0.3	9.0 ± 0.5	4.3 ± 0.3	15.0 ± 2.1	–
P3-3	46.1 ± 1.1	15.3 ± 0.5	7.5 ± 0.4	3.8 ± 0.5	27.2 ± 2.0	–

EDS, energy dispersive spectrometer.
Note: Designations are according to Table 3

(Figure 7) revealed the presence of austenite in the metallic coating. The precipitates were not detected by XRD analysis due to low fraction in the structure. The morphology of the austenite grains varies in different areas of Inconel 625 coatings due to changes in the local solidification conditions. In the fusion boundary region, due to the highest temperature gradient they show a columnar morphology and grow epitaxially from the fusion line opposite to the heat transfer direction. Closer to the

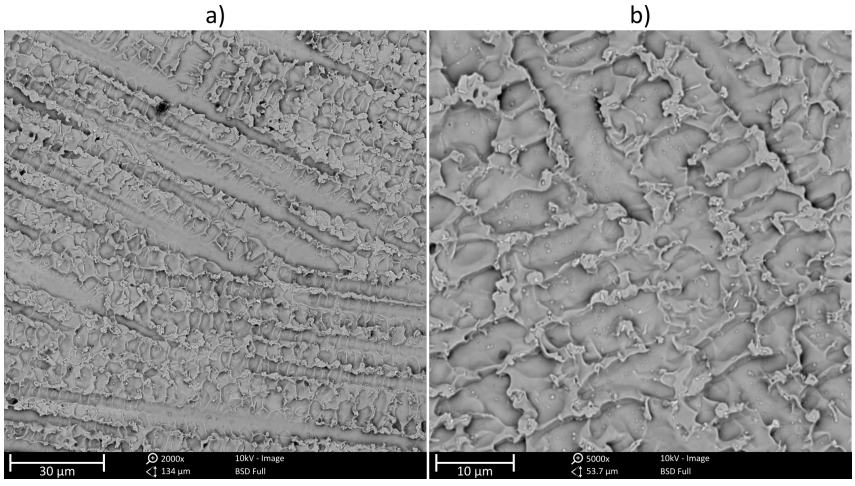


Fig. 4. SEM microstructure of the representative metallic Inconel 625 laser-cladded coating, magnification. (A) Lower magnification. (B) Higher magnification. SEM, scanning electron microscopes

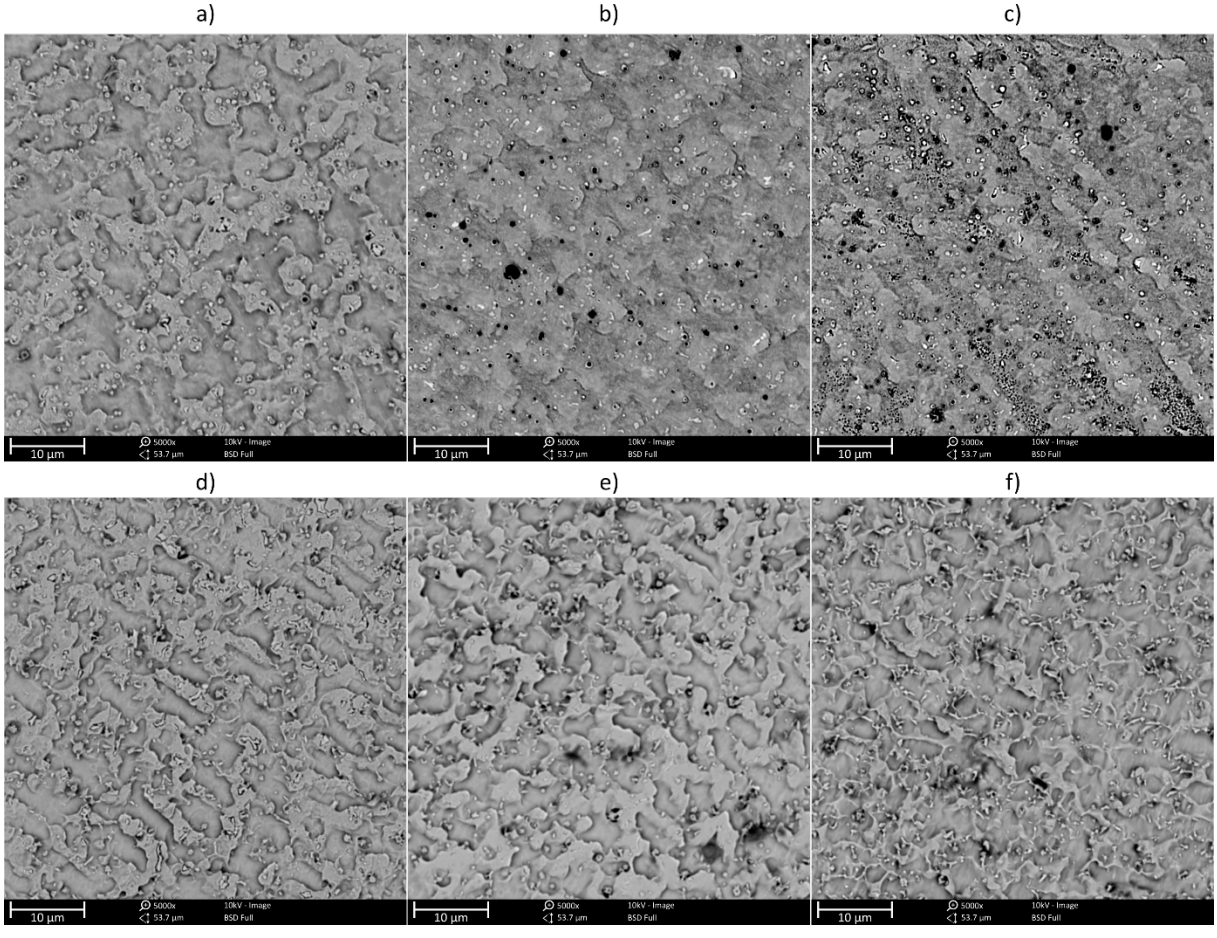


Fig. 5. SEM microstructure of the laser-cladded in situ composite coatings, magnification 5000×. (A) P1-1; (B) P1-2; (C) P1-3; (D) P2-1; (E) P2-2; and (F) P2-3. *Note*: Designations are according to Table 3. SEM, scanning electron microscopes

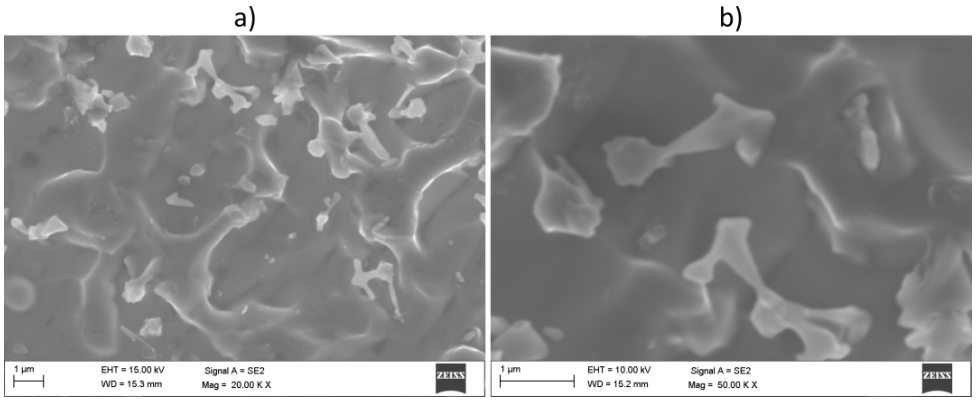


Fig. 6. SEM microstructure of the representative laser-cladded in situ composite coating, magnification. (A) Lower magnification. (B) Higher magnification. SEM, scanning electron microscopes

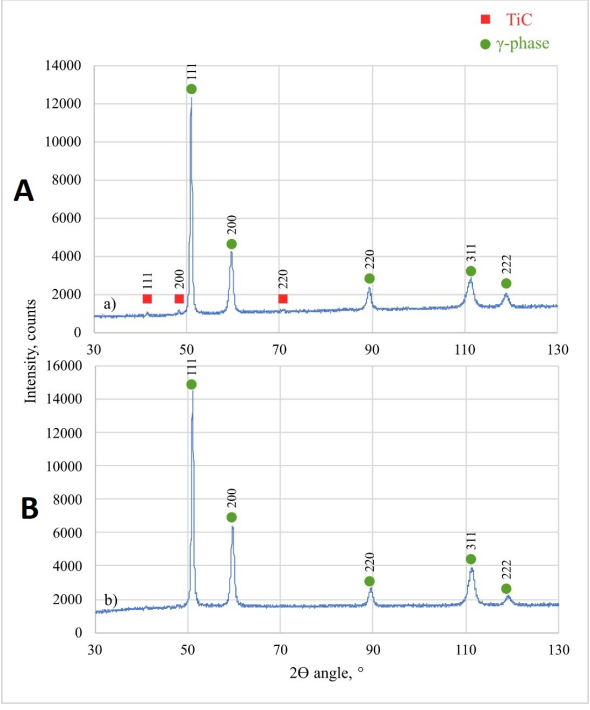


Fig. 7. XRD patterns of (A) representative in situ composite coating and (B) metallic Inconel 625 coating. XRD, X-ray diffraction

coating surface, the temperature gradient becomes lower, which results in the formation of equiaxed dendrites. The addition of titanium and graphite to Inconel 625 powder mixture resulted in microstructural changes that included structural refinement and precipitate formation (Figure 5). The average grain size in the mid-section of the Inconel 625 coatings was 28.7–58.6 µm. In the case of composite coatings depending on the process parameters the average grain size in the mid-section was 10.9–14.2 µm and 10.2–11.3 µm for the P1 and P2 powder mixture, respectively. The grain refinement is related to precipitation during crystallization. As can be observed on the SEM micrographs, in comparison to pure Inconel 625 coatings, the composite coatings contain large amounts of uniformly dispersed particles in the austenite dendrite and interdentritic regions. The observations with higher magnifications (Figure 6) revealed that in the structure, primary blocky precipitates can be observed as well as eutectic precipitates that grow from the primary phases. XRD analysis revealed that the composite coatings are composed of austenite and TiC particles, while EDS analysis revealed that both the primary phases (Figure 8) and eutectic precipitates (Figure 9) contain C, Ti, Nb, and Mo. As can be observed on the SEM micrograph and EDS map (Figure 8), the primary precipitates show gradient distribution of chemical composition, in which the inner, darker part is rich in titanium, which allows to assume that the primary precipitates formed during crystallization as titanium carbides and then, the Nb and Mo dissolved in their crystal lattice. As can be observed in Figure 9, the eutectic precipitates contain less titanium than the primary precipitates. The particle measurements revealed that the increased titanium and graphite content in the powder mixture resulted in the growth of precipitates. For pow-

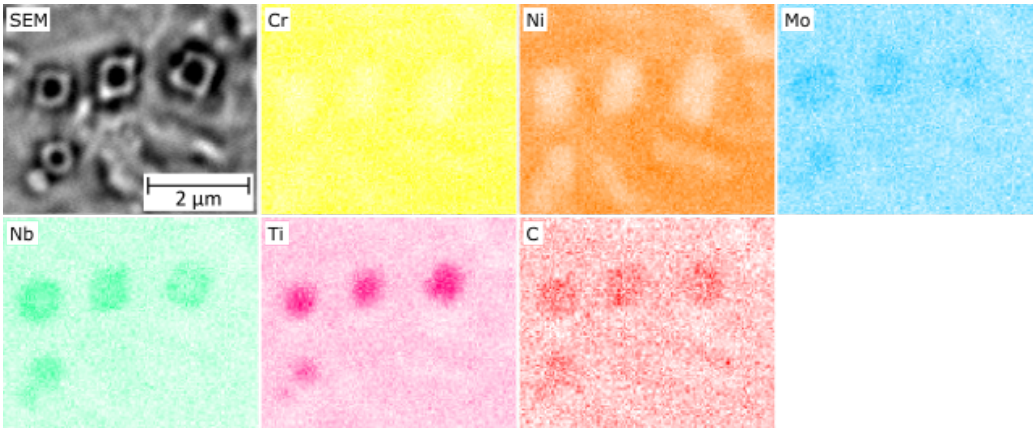


Fig. 8. EDS maps of in situ formed primary reinforcing particles. EDS, energy dispersive spectrometer

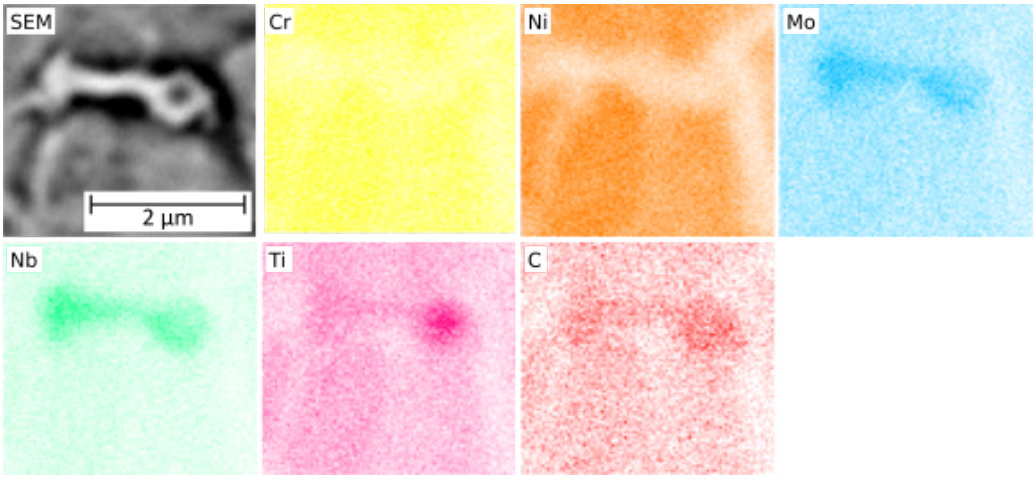
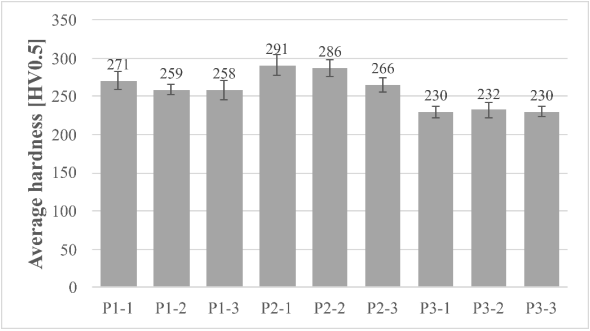


Fig. 9. EDS maps of in situ formed eutectic reinforcing particles. EDS, energy dispersive spectrometer

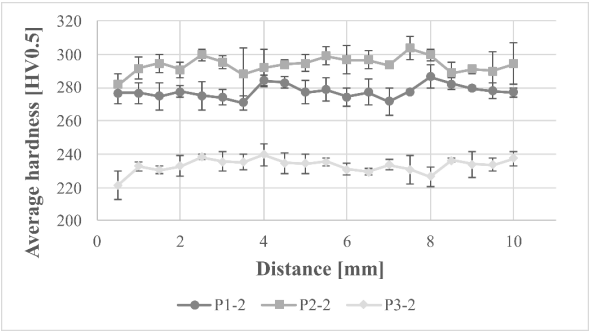
der mixtures with 2.5 vol.% and 5.0 vol.% of titanium and graphite, depending on the process parameters, the maximum primary precipitates size was 0.8–0.9 µm and 1.0–1.6 µm, respectively, and the maximum length of eutectic precipitates was 1.3–2.0 µm and 2.0–2.3 µm, respectively. The microstructure observations in the overlap areas between consecutive beads revealed that no significant microstructure changes appeared in these regions due to additional thermal cycle.

3.3. Hardness analysis

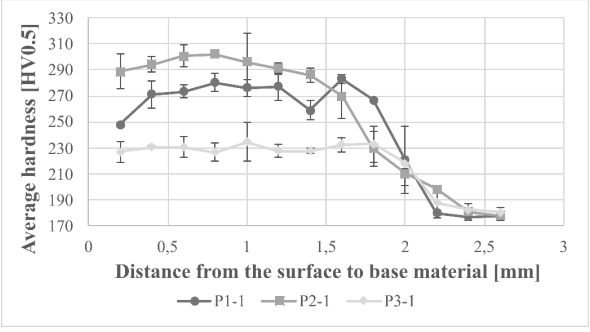
The average hardness results of laser-cladded coatings together with the hardness distribution profiles across the coatings and from the surface to base material are presented in Figure 10. The average hardness of metallic Inconel 625 coatings was about 230–232 HV0.5. The addition of 2.5 vol.% and 5.0 vol.% of titanium and graphite to Inconel 625 powder mixture and related microstructural changes caused the average hardness increase to 258–271 HV0.5 and 266–291 HV0.5, respectively. The average hardness of composite coatings cladded with the use of P2 powder mixture is higher than for P1 powder mixture due to the higher volume fraction of reinforcing particles in the microstructure. Figure 11 shows the influence of the reinforcing particles volume fraction in the microstructure on the average hardness. It is clear that the increase in uniformly distributed reinforcing particles fraction in the structure causes in-



(A)



(B)



(C)

Fig. 10. Hardness results of laser-cladded coatings with standard deviation. (A) Average hardness. (B) Hardness distribution across the multi-pass coatings according to Figure 1A. (C) Hardness distribution from the surface to substrate material according to Figure 1B. *Note*: Designations are according to Table 3

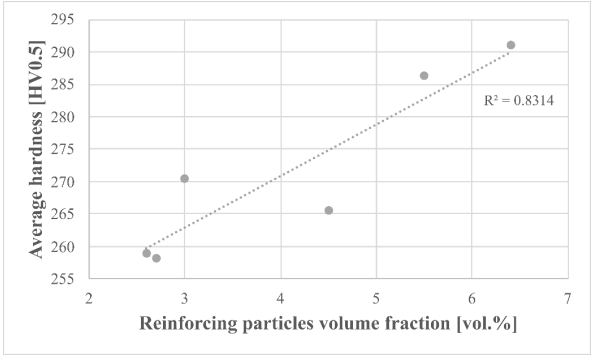


Fig. 11. Influence of reinforcing particles volume fraction on the average hardness of laser-cladded composite coatings

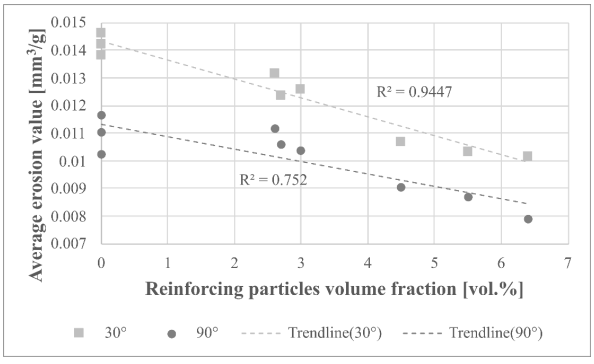


Fig. 12. Influence of reinforcing particles volume fraction on the erosion values of laser-cladded coatings

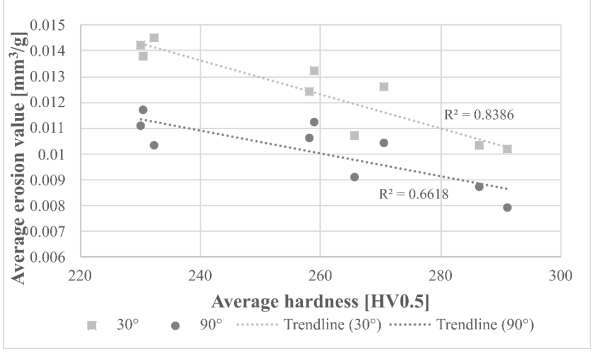


Fig. 13. Influence of average hardness on the erosion values of laser-cladded coatings

crease in the average hardness of composite coatings. As no significant changes were observed in the overlap areas between consecutive beads microstructure, no changes in the hardness profiles in these regions were noted. The hardness profiles of coatings in both the tested directions showed that they have a homogeneous hardness distribution.

Table 6. Average results of erosion rates and erosion values of laser-cladded coatings

Designation	Erosion rate, mg/min		Erosion value, mm^3/g	
	30°	90°	30°	90°
P1-1	0.21 ± 0.05	0.17 ± 0.02	0.0126 ± 0.0032	0.0104 ± 0.0012
P1-2	0.22 ± 0.04	0.19 ± 0.02	0.0132 ± 0.0024	0.0112 ± 0.0013
P1-3	0.21 ± 0.04	0.18 ± 0.02	0.0124 ± 0.0021	0.0106 ± 0.0009
P2-1	0.17 ± 0.03	0.13 ± 0.04	0.0102 ± 0.0018	0.0079 ± 0.0022
P2-2	0.17 ± 0.03	0.14 ± 0.01	0.0103 ± 0.0018	0.0087 ± 0.0007
P2-3	0.18 ± 0.04	0.15 ± 0.03	0.0107 ± 0.0021	0.0091 ± 0.0016
P3-1	0.24 ± 0.04	0.19 ± 0.04	0.0142 ± 0.0021	0.0111 ± 0.0022
P3-2	0.25 ± 0.03	0.21 ± 0.03	0.0146 ± 0.0015	0.0103 ± 0.0015
P3-3	0.23 ± 0.03	0.23 ± 0.02	0.0138 ± 0.0018	0.0117 ± 0.0012

Note: Designations are according to Table 3

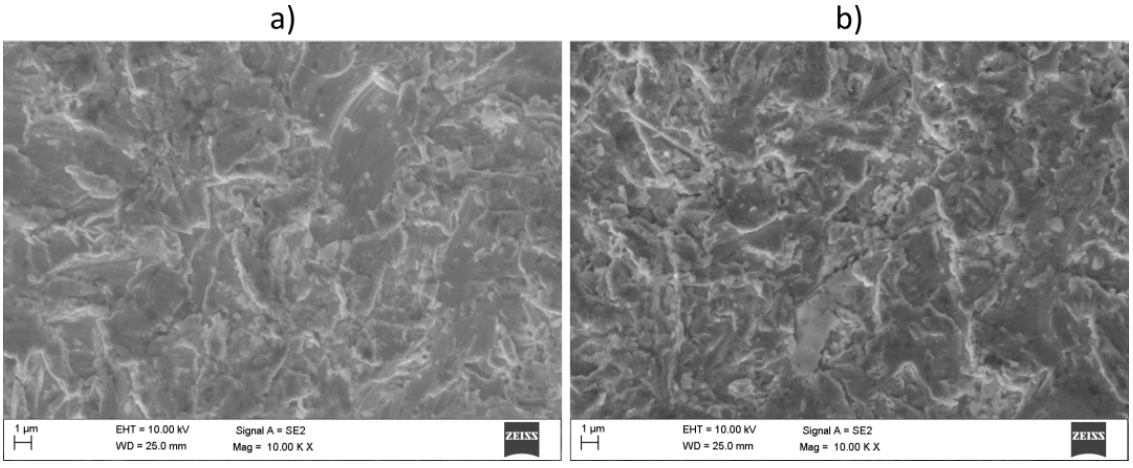


Fig. 14. SEM micrographs of the craters of the representative metallic Inconel 625 coating after solid particle erosion tests. Impingement angles (A) 30° and (B) 90°. SEM, scanning electron microscopes

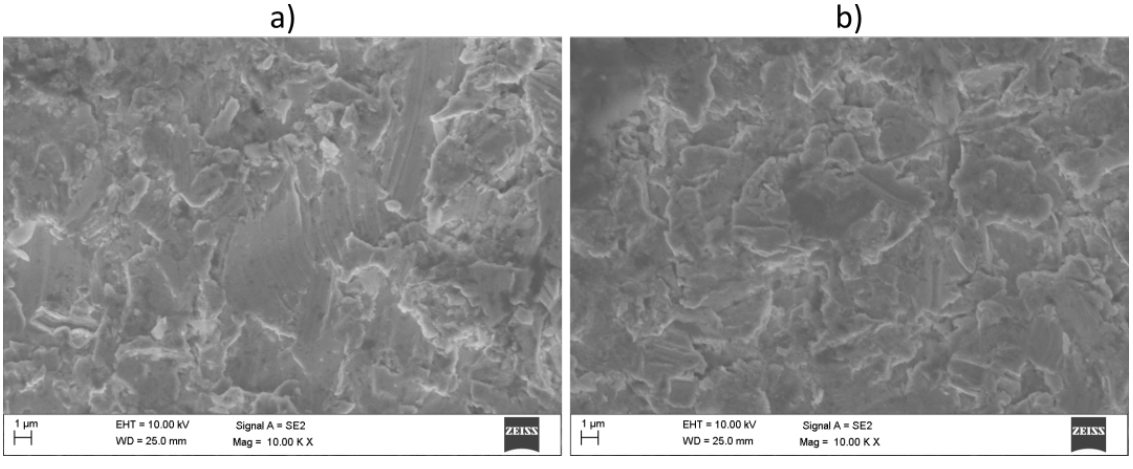


Fig. 15. SEM micrographs of the craters of the representative composite coating after solid particle erosion tests. Impingement angles (A) 30° and (B) 90°. SEM, scanning electron microscopes

3.4. Erosion behavior

The average erosion rates and erosion values received for impingement angles 30° and 90° for laser-cladded coatings are presented in Table 6. For each composite and metallic coating, both erosion rate and value are higher for impingement angle 30° than 90°. Such results are generally characteristic for plastic materials that show a ductile erosion mechanism [30]. The solid particle erosion test results revealed that each of the composite coatings show a lower erosion rate and value in comparison to metallic Inconel 625 coatings, regardless of the laser cladding process parameters and the impingement angles, which proves better erosion resistance. Additionally, the coatings produced with P2 powder mixture, due to the higher volume fraction of reinforcing particles and higher hardness, showed lower erosion rates and values in comparison to coatings cladded with the use of P1 powder mixture. The influence of reinforcing particles volume fraction and hardness on the average erosion value is presented in Figures 12 and 13, respectively. It is clear that with the increased volume fraction of precipitates in the microstructure and average hardness, the erosion resistance improved. No significant changes in erosion rates and values were noted for each used laser cladding process parameters.

The SEM observations of carters received on the coating surfaces after the solid particles were conducted to define the erosion mechanism of metallic (Figure 14) and composite coatings (Figure 15). The metallic Inconel 625 coatings show erosive wear behavior typical for ductile materials, which is in line with the results previously available in the literature [31]. However, as can be observed on the crater micrographs, it is especially noteworthy that the composite coatings show comparable erosive wear behavior under both tested impingement angles. In the case of the 30° impingement angle the scars and narrow grooves can be seen on the eroded surface, indicating that plastic deformation and micro-cutting occurred during erosive test. In the case of the 90° impingement angle the plastic deformation also occurred, however, due to different trajectory of erosive particles in this case, short grooves and craters can be observed on the surface. In the case of the composite coatings, no reinforcing particles can be observed on the SEM micrographs due to their size.

4. Conclusions

Research on the laser cladding of Inconel 625 in situ composite coatings by titanium and graphite addition allowed the following conclusion to be drawn:

- The 2.5 vol.% and 5.0 vol.% of titanium and graphite powders addition to Inconel 625 powder mixture allowed the uniform and high-quality in situ composite coatings production using laser cladding process with the average volume fraction of reinforcing particles in the microstructure 2.6–6.4 vol.%. In comparison to metallic Inconel 625 coatings, the addition of titanium and graphite also caused structure refinement due to precipitation during crystallization.
- The in situ formed reinforcing particles are rich in Ti, Nb, Mo, and C and show blocky and eutectic morphology. The conducted testing allowed to assume that the primary phases precipitated as titanium carbides, and then the niobium and molybdenum dissolved in their crystal lattice. The eutectic precipitates grew on the primary blocky particles.
- The precipitates formation in the structure caused increased hardness (by 12%–27%) and improved solid particle erosion wear resistance (by 10%–30% and 6%–30% in the case of 30° and 90° impingement angle, respectively) of composite coatings in comparison to metallic Inconel 625 coatings. The hardness and erosive wear resistance increased with increase in the reinforcing particles volume fraction. Both metallic and composite Inconel 625-based coatings present ductile mechanism of erosion.

References

[1] Darolia R. Development of strong, oxidation and corrosion resistant nickel-based superalloys: critical review of challenges, progress and prospects. *Int Mater Rev.* 2019;64(6): 355–80. doi:10.1080/09506608.2018.1516713.

[2] Farahmand P, Kovacevic R. Corrosion and wear behavior of laser cladded Ni-WC coatings. *Surf Coat Technol.* 2015;276: 121–35. doi:10.1016/j.surfcoat.2015.06.039.

[3] Deng P, Yao C, Feng K, Huang X, Li Z, Li Y, et al. Enhanced wear resistance of laser cladded graphene nanoplatelets reinforced Inconel 625 superalloy composite coating. *Surf Coat Technol.* 2018;335: 334–44. doi:10.1016/j.surfcoat.2017.12.047.

[4] Chen Y, Lu F, Zhang J, Nie P, Hosseini SRE, Feng K, et al. Laser powder deposition of carbon nanotube reinforced nickel-based superalloy Inconel 718. *Carbon.* 2016;107: 361–70. doi:10.1016/j.carbon.2016.06.014.

[5] Lei J, Shi C, Zhou S, Gu Z, Zhang LC. Enhanced corrosion and wear resistance properties of carbon fiber reinforced Ni-based composite coating by laser cladding. *Surf Coat Technol.* 2018;334: 274–85. doi:10.1016/j.surfcoat.2017.11.051.

[6] Janicki D, Musztyfaga-Staszuk M. Direct diode laser cladding of Inconel 625/WC composite coatings. *Stroj Vestn/J Mech Eng.* 2016;62(6): 363–72. doi:10.5545/sv-jme.2015.3194.

[7] Hong C, Gu D, Dai D, Gasser A, Weisheit A, Kelbassa I, et al. Laser metal deposition of TiC/Inconel 718 composites with tailored interfacial microstructures. *Opt Laser Technol.* 2013;54: 98–109. doi:10.1016/j.optlastec.2013.05.011.

[8] Pizzatto A, Teixeira MF, Rabelo A, Falcade T, Scheid A. Microstructure and wear behavior of NbC-reinforced Ni-based alloy composite coatings by laser cladding. *Mater Res.* 2021;24(3): e20200447. doi:10.1590/1980-5373-MR-2020-0447.

[9] Yu T, Tang H. Microstructure and high-temperature wear behavior of laser clad TaC-reinforced Ni-Al-Cr coating. *Appl Surf Sci.* 2022;592: 153263. doi:10.1016/j.apsusc.2022.153263.

[10] Janicki D. Laser cladding of Inconel 625-based composite coatings reinforced by porous chromium carbide particles. *Opt Laser Technol.* 2017;94: 6–14. doi:10.1016/j.optlastec.2017.03.007.

[11] Xu Z, Xie Y, Ebrahimnia M, Dang H. Effect of B4C nanoparticles on microstructure and properties of laser cladded IN625 coating. *Surf Coat Technol.* 2021;416: 127154. doi:10.1016/j.surfcoat.2021.127154.

[12] Muvvala G, Karmakar DP, Nath AK. Online assessment of TiC decomposition in laser cladding of metal matrix composite coating. *Mater Des.* 2017;121: 310–20. doi:10.1016/j.matdes.2017.02.061.

[13] Chen L, Yu T, Chen X, Zhao Y, Guan C. Process optimization, microstructure and microhardness of coaxial laser cladding TiC reinforced Ni-based composite coatings. *Opt Laser Technol.* 2022;152: 108129. doi:10.1016/j.optlastec.2022.108129.

[14] Kotarska A, Poloczek T, Janicki D. Characterization of the structure, mechanical properties and erosive resistance of the laser cladded Inconel 625-based coatings reinforced by TiC particles. *Materials.* 2021;14: 2225. doi:10.3390/ma14092225.

[15] Kołodziejczak P, Bober M, Chmielewski T. Wear resistance comparison research of high-alloy protective coatings for power industry prepared by means of CMT cladding. *Appl. Sci.* 2022;12: 4568. doi:10.3390/app12094568.

[16] Czupryński A, Mele C. Properties of flame spraying coatings reinforced with particles of carbon nanotubes. *Adv Mater Sci.* 2021;21(1): 57–76. doi:10.2478/adms-2021-0005.

[17] Kotarska A. The laser alloying process of ductile cast iron surface with titanium. *Metals.* 2021;11(2): 282. doi:10.3390/met11020282.

[18] Poloczek T, Janicki D, Górka J, Kotarska A. Effect of Ti and C alloyants on the microstructure of laser cladded cobalt-chromium coatings. *IOP Conf Ser Mater Sci Eng.* 2021;1182: 012063. doi:10.1088/1757-899X/1182/1/012063.

[19] Janicki D. In-situ synthesis of titanium carbide particles in and iron matrix during diode-laser surface alloying of ductile cast iron. *Mater Technol.* 2017;51(2): 317–21. doi:10.17222/mit.2015.198.

[20] Lont A, Górka J, Janicki D, Matus K. The laser alloying process of ductile cast iron surface with titanium powder in nitrogen atmosphere. *Coatings.* 2022;12(2): 227. doi:10.3390/coatings12020227.

[21] Shuting S, Hanguang F, Xuelong P, Xingye G, Jian L, Yongping L, et al. Effect of liquid nitrogen cooling on grain growth and properties of laser cladding in-situ (Ti, Nb)C/Ni composite coatings. *Mater Charact.* 2019;152: 115–29. doi:10.1016/j.matchar.2019.04.012.

[22] Chen L, Zhao Y, Meng F, Yu T, Ma Z, Qu S, et al. Effect of TiC content on the microstructure and wear performance of in situ synthesized Ni-based composite coatings by laser direct energy deposition. *Surf Coat Technol.* 2022;444: 128678. doi:10.1016/j.surfcoat.2022.128678.

[23] Gao Z, Geng H, Qiao Z, Sun B, Gao Z, Zhang C. In situ TiB_X/Ti_XNi_Y/TiC reinforced Ni60 composites by laser cladding and its effect on the tribological properties. *Ceram Int.* 2023;49: 6409–18. doi:10.1016/j.ceramint.2022.10.087.

[24] Wu F, Chen T, Wang H, Liu D. Effect of Mo on microstructures and wear properties in situ synthesized Ti(C,N)/Ni-based composite coatings by laser cladding. *Materials.* 2017;10: 1047. doi:10.3390/ma10091047.

[25] Muvvala G, Karmakar DP, Nath AK. In-process detection of microstructural changes in laser cladding of in-situ Inconel 718/TiC metal matrix composite coating. *J Alloys Compd.* 2018;740: 545–58. doi:10.1016/j.jallcom.2017.12.364.

[26] ASTM International. E407-99. *Standard practice for microetching metals and alloys.* PA, USA; 1999.

[27] ASTM International. G76-04. *Standard test method for conducting erosion tests by solid particle impingement using gas jets.* PA, USA; 2004.

[28] Cieslak MJ, Headley TJ, Romig AD, Kollie T. A melting and solidification study of alloy 625. *Metall Trans A.* 1988;19A: 2319–31. doi:10.1007/BF02645056.

[29] Cieslak MJ. The welding and solidification metallurgy of alloy 625. *Weld J.* 1991;70: 49–56.

[30] Stachowiak GW, Batchelor AW. *Engineering tribology.* Oxford: Butterworth-Heinemann; 2014. p. 551–6.

[31] Solecka M, Kopyściański M, Kusiński J, Kopia A, Radziszewska A. Erosive wear of Inconel 625 alloy coatings deposited by CMT method. *Arch Metall Mater.* 2016;61(2B): 1201–6. doi:10.1515/amm-2016-0199.

Received 2022-12-20
Accepted 2023-01-08